HHS Public Access

Author manuscript

J Opt Soc Am B. Author manuscript; available in PMC 2018 January 29.

Published in final edited form as:

J Opt Soc Am B. 2017 ; 34(5): B64–B77.

Tomographic phase microscopy: principles and applications in bioimaging [Invited]

Di Jin[1,2,†], **Renjie Zhou**[2,†,*], **Zahid Yaqoob**[2], and **Peter T. C. So**[1,2,3]

[1]Department of Mechanical Engineering, Massachusetts Institute of Technology, Cambridge, Massachusetts 02139, USA

[2]Laser Biomedical Research Center, G. R. Harrison Spectroscopy Laboratory, Massachusetts Institute of Technology, Cambridge, Massachusetts 02139, USA

[3]Department of Biological Engineering, Massachusetts Institute of Technology, Cambridge, Massachusetts 02139, USA

Abstract

Tomographic phase microscopy (TPM) is an emerging optical microscopic technique for bioimaging. TPM uses digital holographic measurements of complex scattered fields to reconstruct three-dimensional refractive index (RI) maps of cells with diffraction-limited resolution by solving inverse scattering problems. In this paper, we review the developments of TPM from the fundamental physics to its applications in bioimaging. We first provide a comprehensive description of the tomographic reconstruction physical models used in TPM. The RI map reconstruction algorithms and various regularization methods are discussed. Selected TPM applications for cellular imaging, particularly in hematology, are reviewed. Finally, we examine the limitations of current TPM systems, propose future solutions, and envision promising directions in biomedical research.

1. INTRODUCTION

In the 1960s, after the invention of lasers, several groups pioneered digital holography (DH) to numerically record and process holographic data with the aid of a digital camera and a computer [1,2]. In the 1990s, as image sensors became widely available, Schnars and Jüptner pioneered the use of CCD cameras in off-axis DH systems. On the other hand, phase contrast (PC), discovered around the same time as holography in the 1940s, gradually gained popularity as a microscopic technique for viewing transparent biological specimen without staining [3]. In the mid-1990s, several works on integrating PC with DH made quantitative analysis and reconstruction of microscopic structures possible, marking the beginning of a new field, called quantitate phase imaging (QPI) [4,5]. In most cases, the terms quantitative PC imaging, digital holographic microscopic imaging, and interference microscopic imaging

*Corresponding author: renji@mit.edu.

†These authors contributed equally to this work.

OCIS codes: (050.1960) Diffraction theory; (180.1655) Coherence tomography; (100.6950) Tomographic image processing; (100.3200) Inverse scattering; (100.5070) Phase retrieval; (180.3170) Interference microscopy.

are used interchangeably with QPI. In this review of tomographic phase microscopy (TPM), we use the terminology QPI and specify it as a microscopy method that retrieves phase maps of biological samples from complex field measurements with interferometry. Over the past two decades, QPI has gained great popularity as a label-free microscopic technique for biological imaging [6–13].

Although QPI has been successfully used for many cellular and tissue studies, the fact that phase is a product of thickness and average RI can potentially result in inaccurate interpretations of QPI data when imaging complex three-dimensional (3D) structures. In order to gain more accurate morphological information such as nuclear shape, nuclear dry mass, and nuclear-to-cytoplasm volume ratio, depth-resolved [14–16] or tomographic versions of QPI [17–19], i.e., TPM, are often desired. In this paper, we will cover the developments of TPM. In 2006 and 2007, two groups reported the first implementations of TPM for 3D imaging of cells by quantitatively mapping their RI distributions [17,18]. In those early works, the 3D reconstruction physical model was based on a back filtered projection method, similar to what was used in x-ray computed tomography (CT). It assumed phase measurement to be an integration of RI along the projection angle, which ignored the significance of the optical diffraction effect, thus limiting the earlier TPM systems for small sample RI variations over the wavelength scale. In cell imaging experiments, this inaccurate tomography model can significantly affect the 3D reconstruction resolution, especially for cells that are much thicker than the depth of field of the imaging systems [20].

In the 1960s, Wolf proposed the idea of using holography for 3D object reconstruction by developing a diffraction-based tomography model, known as optical diffraction tomography (ODT) [21]. However, this concept was not implemented to TPM for 3D imaging of cells until 2009 [20]. Since then, there have been numerous developments in ODT [22–26]. The early TPM systems were mostly based on incident laser illumination angle scanning with the help of galvanometer mirrors or sample rotations to obtain projection field measurements [17,18,20,27]. As new hardware techniques became available, spatial light modulators [28–30], digital micromirror devices (DMDs) [31], super-continuum lasers [32,33], fast cameras [34], and graphics-processing units [35] have been integrated into TPM systems to achieve improved imaging stability and speed. For high-throughput 3D cell measurements, microfluidic devices have also been integrated into TPM [34,36]. Although hardware improvements are important, there still are physical limitations that affect the performance of TPM. Current TPM techniques are based on transmission measurements that have a common *missing cone problem* like other wide-field microscopy methods [37,38]. Reflection-type TPM systems could potentially solve this problem by providing high axial sectioning capability [39]. Additionally, laser-based coherent TPM systems suffer from a small depth of field and speckle noise, which can be solved using incoherent light. The statistical property of incoherent light sources can naturally create optical sectioning effects across the focus plane through coherence gating, which is the physical basis of optical coherence tomography (OCT) [40]. Through a simple scanning of the sample through the objective focus, 3D maps of sample RI can be obtained, as was demonstrated in white-light diffraction tomography in 2014 [41]. Most recently, advanced image-processing tools, including total variation (TV) regularization [42,43] and 3D deconvolution algorithms

[41,44,45], have been applied to ODT to overcome the hardware and physical limits. For example, regularized ODT models that use sample priori information, such as non-negativity and piecewise smoothness, have been implemented to alleviate the missing cone issue in TPM [24,46,47]. In 2015, a new physical model, based on the beam propagation method (BPM) to treat light diffraction, was demonstrated for 3D RI reconstruction in TPM [43,48]. This work has pioneered the machine learning concept for TPM [49].

As the TPM technique advances and matures, it has been increasingly applied to biomedical research. One of the most extensively applied areas is hematology [50,51] where TPM is used to study the morphological alterations of red blood cells (RBCs) and the related diseases caused by parasitic protozoa, such as *Plasmodium falciparum* [52,53] and *Babesia microti* [54]. TPM has also been used to measure eukaryotic cell biophysical markers, such as overall shape and volume [26,36], and dry mass [19,36]. Worth mentioning is that TPM is able to extract the properties of subcellular organelles such as nucleus [34,50] and lipid droplets (LDs) [55]. In this review, we will cover the aforementioned recent developments in TPM. It will focus on three aspects of TPM: (1) physical reconstruction model developments, (2) computational 3D reconstruction algorithms, and (3) bioimaging applications.

2. PHYSICAL MODELS FOR RI RECONSTRUCTION

By treating a 3D object as a black box and performing multiple intensity or field measurements through different ways, one is expected to be able to retrieve the 3D structure (i.e., RI maps) of the object by solving the *inverse scattering* problem. In the early days, inspired by the x-ray CT technique, optical physicists developed methods to reconstruct the RI distributions of microscopic objects through angle scanning of a laser illumination beam across the object (or rotate the object). In one of the earliest optical tomography experiments, Snyder and Hesselink [56] demonstrated the mapping of the RI distribution of a glass rod with holographic measurements; their reconstruction was done with a filtered back projection diffraction tomography algorithm developed by Devaney [57]. It was well understood that high-fidelity 3D reconstruction algorithms need to take into account the optical diffraction phenomenon [21,57–60]. The concept of tomographic phase microscopy or TPM was first proposed in 2007 as a technique to measure the RI maps of living cells with digital holographic microscopy [18]. In 2009, Sung *et al.* introduced a Rytov approximation-based ODT model for cell RI reconstruction in TPM [20], which enabled higher 3D resolution than the earlier experiments based on filtered back projection algorithms that ignored diffraction [17,18]. In Sections 2.A–2.C, we will discuss the reconstruction physical models in the context of ODT for coherent and incoherent illuminations.

A. Coherent Illumination ODT Reconstruction

As described in Fig. 1, the physical structure of an object is described by the object scattering potential function $\chi(x,y,z)=\beta_0^2[n^2(x,y,z)-n_m^2]$ where $\beta_0 = 2\pi/\lambda_0$ is the propagation constant in free space, λ_0 is the illumination wavelength in free space, $n(x, y, z)$ is the RI distribution of the object (the parameter to be determined), and n_m is the RI of the

surrounding medium. With a plane wave incident on the object, scattered fields are generated in both forward and the backward directions. The scattered field, U_s, is described by the following inhomogeneous wave equation [21]:

$$\nabla^2 U_s(\mathbf{r})+\beta^2 U_s(\mathbf{r})=-\chi(\mathbf{r})U(\mathbf{r}), \quad (1)$$

where $\beta = n_m\beta_0$ is the propagation constant in the medium and $U(\mathbf{r})$ is the total field that has contributions from the incident field plane wave, $U_i(\mathbf{r})$, and the scattered field, $U_s(\mathbf{r})$, i.e., $U(\mathbf{r}) = U_i(\mathbf{r}) + U_s(\mathbf{r})$. Two approximations have been used here to solve the scattered field in Eq. (1). The first approximation, also called the first Born approximation, which assumes that $U_s(\mathbf{r}) \ll U_i(\mathbf{r})$ results in $U(\mathbf{r}) \approx U_i(\mathbf{r}) = e^{i\mathbf{k}_i\cdot\mathbf{r}}$, where $\mathbf{k}_i = \beta\hat{\mathbf{k}}_i = (k_{xi}, k_{yi}, k_{zi})$ is the incident wave vector and $\hat{\mathbf{k}}_i$ is the direction unit vector with $\hat{\mathbf{k}}_i = (\hat{k}_{xi}, \hat{k}_{yi}, \hat{k}_{zi})$. In the medium, where the incident field emerges, the dispersion relation establishes that $k_{xi}^2+k_{yi}^2+k_{zi}^2=\beta^2=n_m^2\beta_0^2$. Through a wave-vector space method [41,61] or a Green's function approach [21], the scattered field is solved in the transverse Fourier space for a particular focal plane z (z =0 is the imaging plane) as

$$U_s(k_x,k_y;z)=\frac{e^{\pm iqz}}{q}\chi(k_x-k_{xi},k_y-k_{yi},\pm q-k_{zi}), \quad (2)$$

where "+q" represents the forward scattered field and "−q" represents the backward scattered field; k_x and k_y represent the scattered field transverse spatial frequencies; and $q=\sqrt{\beta^2-k_x^2-k_y^2}$ is the axial spatial frequency projection of the scattered field. For simplicity in the formulation, we are using the variables of a function to indicate the exact transformation domain. Equation (2) reveals the relationship between the scattered field and scattering potential in a Fourier transform relation, which can also be written in the integral form of the Lipmann–Schwinger equation. The inverse scattering solution to the object function is therefore given by (Wolf [21])

$$\chi(U,V,W)=\frac{q}{e^{\pm iqz}}U_s(k_x,k_y;z). \quad (3)$$

where $U = k_x - k_{xi}$, $V = k_y - k_{yi}$, and $W = \pm q - k_{zi}$; "+q" represents the forward solution. The measurement is usually performed at the imaging plane, and, thus, $\chi(U, V, W) = qU_s(k_x, k_y; z = 0) = q \cdot \Im_{2D}[U_s(x, y; z = 0)]$, where $\Im_{2D}$ represents the two-dimensional (2D) Fourier transform. According to this equation, each measurement of $U_s(x, y; z = 0)$can be mapped to a particular spherical surface on the Ewald sphere in (U, V, W) space. As illustrated in Fig. 2(a), through changing the illumination angle on the sample, i.e., changing the pair k_{xi} and k_{yi} and mapping the corresponding scattered field into the Ewald sphere in the "mapped region" in Fig. 2(b), we can eventually recover a 3D spatial frequency region for $\chi(U, V, W)$. In order to better illustrate the Ewald sphere mapping, we have sketched the

frequency sections from seven different illumination angles (−64°, −37°, −18°, 0°, 18°, 37°, and 64° as indicated by different colors) in Fig. 2(b). After a complete mapping, with a 3D inverse Fourier transform of $\chi(U, V, W)$, the 3D object function in real space can be obtained, which will allow us to obtain its RI map. However, as shown in Fig. 2(b), we cannot recover the central low frequency (in U and V) region of the 3D Fourier space, which is called the missing cone problem. Reflection-mode measurements can fill the missing cone region as shown in Fig. 2(b), where we have mapped the back scattered fields corresponding to different illumination angles into the Ewald sphere (the same illumination angles as in transmission-mode mapping are used). However, building an angle scanning reflection-mode TPM experimental system for biological imaging is very difficult, mainly because the back scattered fields from the cellular structures are very weak due to the small RI contrast of about 0.03. The detector will be mostly saturated by the background reflection from the sample holders such as cover glasses. In contrast, incoherent illumination with a broadband source or speckle field, as well as confocal-based illumination, can potentially make a better reflection-mode TPM with the help of the coherence gating or confocal gating effect. Recently, several versions of reflection-mode QPI systems have demonstrated inherent depth discrimination [14], which can be potentially incorporated into new TPM approaches to enable recovery of information from these missing regions [39,62,63].

The first Born approximation is valid when the total phase delay of the field is small and there is substantially low optical absorption, which means that it works well for thin objects with weak RI contrasts to the media. For relatively thick objects, the Rytov approximation is more appropriate, which assumes that the total field has a complex phase function $\phi_s(\mathbf{r})$which is related to the scattered field, i.e., $U(\mathbf{r}) = e^{\phi_i(\mathbf{r})+\phi_s(\mathbf{r})} = U_i(\mathbf{r})e^{\phi_s(\mathbf{r})}$ {refer to Eq. (5) in [58]}. Note that both approximations assume weak RI variations and single scattering events in the sample, which is mostly true for imaging single cells. In order to image strong scattering samples with TPM such as tissues, aberration corrections may be needed. As derived in Ref. [20], under the Rytov approximation, the reconstruction still follows Eq. (3), except that the scattered field U_s is replaced with $U_s(\mathbf{r}) = U_i(\mathbf{r}) \ln(U(\mathbf{r})/U_i(\mathbf{r}))$, and $U(\mathbf{r})$ can be measured from a QPI system. We note that the Rytov approximation is valid when the gradient of the RI is small, which means the objects need to be smooth in RI distribution (see page 485 in Ref. [64] for more details).

In TPM systems using coherent illumination ODT models, the experiments have been mostly based on angle scanning of coherent laser illuminations. Recently, with the availability of more advanced super-continuum laser sources, wavelength scanning TPM has also been demonstrated [32]. Its reconstruction physical model is similar to the angle scanning case, and details can be found in Ref. [32].

B. Coherence-Gated ODT Reconstruction

In coherent illumination ODT, the 3D object reconstruction is performed with Fourier space mapping. For incoherent illumination ODT, one can selectively image different sample depths through creating an optical sectioning effect, i.e., achieving coherence-gated ODT. The optical sectioning is a result of the 3D confinement of optical fields, i.e., the coherence gating effect. There are two ways to create the coherence gating effect in TPM. The first one

is through using temporally incoherent illumination via a broadband light source, similarly to OCT [40]. The second option is to utilize spatially incoherent illumination with dynamic speckle fields [14,65] or confocal laser scanning [63,66]. Earlier work has used spatially or temporally incoherent illumination to achieve depth-resolved quantitative phase measurements [67–69]. In order to apply those systems to TPM, one may need to consider the phase measurement accuracy [70], as it can be affected by the dispersion and aberration from incoherent illumination, which may result in deviated 3D RI mappings. The 3D reconstruction models for both types of incoherent illuminations have been addressed very recently [39,41,61]. In Sections 2.B.1 and 2.B.2, we will briefly introduce the 3D reconstruction models for both temporal and spatial incoherent illuminations.

1. Temporally Incoherent Illumination—In interferometric imaging, the measurement is the cross-correlation function between the scattered field, U_s, and the reference field, U_r. For a broadband light source, it has a short temporal coherence length, which will help to create a narrow temporal cross-correlation function. The width of this function determines the depth selectivity in TPM. Next, we formulate the 3D reconstruction model under temporally incoherent illumination. The temporal cross-correlation function, $\Gamma_{12}(\mathbf{r}, \tau)$, at each spatial point is a function of temporal delay, τ,

$$\Gamma_{12}(\mathbf{r},\tau)=\langle U_s(\mathbf{r},t)U_r^*(\mathbf{r},t+\tau)\rangle_t, \quad (4)$$

where $\langle\rangle_t$ is an ensemble average over time. We can relate $\Gamma_{12}(\mathbf{r}, \tau)$ to the cross-spectral density function, $W_{12}(\mathbf{r}, \omega)$, through a Fourier transform by using the generalized Wiener–Khintchine theorem [71,72],

$$\Gamma_{12}(\mathbf{r},\tau)=\int_0^\infty W_{12}(\mathbf{r},\omega)e^{i\omega\tau}\mathrm{d}\omega, \quad (5)$$

where $W_{12}(\mathbf{r},\omega)=\langle U_s(\mathbf{r},\omega)U_r^*(\mathbf{r},\omega)\rangle$. Normally, phase measurements are performed around zero delay, i.e., $\tau = 0$. The scattered field solutions for broadband source illumination are similar to the ones given in Eq. (2), but modified to incorporate the source spectrum [41]. For the transmission-mode TPM operation, using the forward scattering field solution, the integral in Eq. (5) can be evaluated to give the following reconstruction model:

$$\chi(U,V,W)=\frac{\Gamma_{12}(U,V,W)}{\sum(U,V,W)}, \quad (6)$$

where $U = k_x$, $V = k_y$, and $W=q-\beta=\sqrt{\beta^2-k_x^2-k_y^2}-\beta$ are the object frequency support, and $\Sigma(U, V, W)$ is the 3D coherent transfer function (CTF) given by

$$\sum(U,V,W)=[(W^2+k_\perp^2)^2/W^3]S[-(W^2+k_\perp^2)/2W], \quad (7)$$

which is determined by the source spectrum S and the numerical aperture (NA) of the imaging system that limits the maximum value of $k_\perp$. The transfer function determines the lateral and axial imaging resolution of the tomographic imaging system. As an example, Fig. 3(a) shows the transfer function of a broadband illumination TPM system with a halogen lamp source that has 1.2 μm temporal coherent length and an imaging NA of 1.4 [41]. The 3D point-spread function (PSF) is calculated from the transfer function. Cross-section planes x–y ($z = 0$) and x–z ($y = 0$) are shown in Fig. 3(c) and 3(d), respectively. The full width at half-maximum (FWHM) values of the PSF in the lateral and axial dimensions closely match the lateral resolution and temporal coherence length values.

Like in coherent illumination reconstruction, the incoherent illumination transmission-mode model also has the missing cone problem. In reflection-mode reconstruction, it is expected to have a better sectioning capability and suffer no missing cone. However, it is very difficult to build a reflection-mode TPM system with broadband illumination as the reflected signal is very weak. Lasers have high power, and, thus, using them as illumination sources for reflection-mode phase measurements would enable high phase signal contrast. In the next section, we discuss how to use spatially incoherent monochromatic light as illumination for 3D imaging in TPM.

2. Spatially Incoherent Illumination—A monochromatic light source, such as a laser, can generate 3D patterned illumination through a multimode fiber (it generates speckle fields) and a grating to achieve 3D field confinement; this was demonstrated in wide-field fluorescence microscopy by Gustafsson *et al.* [38]. Recently, dynamic speckle field illumination has been implemented to achieve depth selectivity or depth sectioning in quantitative phase microscopes (QPMs) [14,73]. However, no reconstruction models have yet been fully developed for dynamic speckle illumination-based TPM systems. Recently, the depth sectioning effect in reflection-mode dynamic speckle QPM has been modeled [39]. Here we give a summary of the results in [39], which can potentially provide a guide on developing tomographic reconstruction models in TPM under such illumination sources. In this type of an incoherent illumination QPM system, the spatial cross-correlation function, $\Gamma_{12}(z_R; k_{xi}, k_{yi})$ along the focal axis (x, y is not considered in [39] by assuming a one-dimensional object) for each speckle component, (k_{xi}, k_{yi}), is

$$\Gamma_{12}(z_R;k_{xi},k_{yi})=\frac{P^2(k_{xi},k_{yi})e^{ik_{zi}(2z_R)}}{k_{zi}}, \quad (8)$$

where z_R is the defocus position, $P(k_{xi}, k_{yi})$ is the speckle distribution over the back aperture of the imaging objective, and $k_{zi}=\sqrt{\beta^2-k_{xi}^2-k_{yi}^2}$ through the dispersion relation. By

integrating over all the speckle components (k_{xi}, k_{yi}) over the back aperture, we obtain the overall spatial correlation function as

$$\mathrm{Re}(\Gamma_{12})=\mathrm{sinc}\left(\frac{2\beta z_R}{\pi}\right)-\cos\theta_{\max}\,\mathrm{sinc}\left(\frac{2\beta\cos\theta_{\max} z_R}{\pi}\right), \quad (9)$$

where $\theta_{\max}$ is the maximum speckle illumination angle in the object space, and the sinc function is defined as $\mathrm{sinc}(x)=\sin(\pi x)/\pi x$. For an 800 nm speckle illumination QPM system with an NA = 1.0 imaging objective, we can calculate the spatial correlation function and determine the depth sectioning as shown in Fig. 4. The FWHM value of depth sectioning or depth resolution is determined to be 1.06 μm. It has been found that the depth resolution follows a λ/NA^2 law.

C. Beam Propagation Model-Based Reconstruction

In the Born or Rytov approximation-based tomographic reconstruction models covered in Sections 2.A and 2.B, we have to assume weak light scattering or single scattering in the unknown objects. A BPM-based tomographic reconstruction model, proposed by Kamilov *et al.* [43,48], allows considering multiple scattering events by dividing the object into multiple layers and subsequently forming an artificial neural network geometry to model the RI distribution. Therefore, the BPM reconstruction model applies to thicker or highly inhomogeneous biological objects. Instead of using iterative phase retrieval [59,74], the RI reconstruction in [43,48] uses complex field measurements from a typical angle scanning TPM system [18]. In the following paragraphs, we briefly introduce the concepts of retrieving RI distributions using the BPM model.

In the BPM model, an inhomogeneous sample is virtually divided into thin slices along the propagation direction z. Light propagation is modeled as phase modulation based on the paraxial wave equation. After each layer, the optical field is described as [43]

$$u(\mathbf{r})=a(\mathbf{r})e^{i\beta_0 n_m z}, \quad (10)$$

where $a(\mathbf{r})$ is a complex envelope function that models light diffraction in each sample layer. The sample RI distribution $n(\mathbf{r})$ is decomposed into a constant medium n_m and a perturbation $\delta n(\mathbf{r})$ due to inhomogeneity. Therefore, the propagation constant in the sample, $\beta_s(\mathbf{r})$, is written as

$$\beta_s(\mathbf{r})=\beta_0 n(\mathbf{r})=\beta_0(n_m+\delta n(\mathbf{r})). \quad (11)$$

The complex envelope $a(\mathbf{r})$ evolves along the optical axis as [43,75]

$$a(x,y,z+\delta z)=e^{i\beta_0\delta n(\mathbf{r})\delta z}\times\Im_{2\mathrm{D}}^{-1}\left\{\Im_{2\mathrm{D}}(a(x,y,z))\times e^{-i\left(\frac{k_x^2+k_y^2}{\beta_0 n_m+\sqrt{\beta_0^2 n_m^2-k_x^2-k_y^2}}\right)\delta z}\right\}, \quad (12)$$

where δz is the step size or sample slice size along z direction. The right-hand side of this equation can be decomposed into two parts: the first term $e^{i\beta_0\delta n(\mathbf{r})\delta z}$ takes refraction into account, whereas the other term deals with the diffraction. By repeatedly using this equation step-by-step, we can get to know how the complex field evolves after propagating over an arbitrary distance along the optical axis. In other words, once given the initial condition, the optical field distribution can be obtained anywhere in space (note that reflected light has not been considered in the current BPM model). Compared with the ODT reconstruction model, BPM no longer uses the scattering potential to represent the RI in a quadratic function. Instead, it directly seeks an equation to link RI and the measured electromagnetic field, which makes the BPM model nonlinear. Compared with its linear counterpart, this nonlinear physical model can be more accurate when the scattering effects are strong. Kamilov *et al.* [43,48] successfully demonstrated the tomographic reconstruction of RI distribution by iteratively minimizing the error between the measured field and estimated field computed based on BPM; they used the complex field measurements from an angle scanning TPM system.

3. REGULARIZED TPM

In TPM systems based on the laser beam angle scanning technique, the range of illumination angle is limited to around 60° by the NA of the condenser lens. The same situation also applies to TPM systems employing an object in motion, where a high-NA condenser lens is used to create a line-focused beam, which can be viewed as a combination of infinite plane waves of a limited range of illumination angles [36]. Correspondingly, in the 3D Fourier domain, the coverage of accessible spatial frequency along k_z, which determines the focus sectioning capability, is limited. Additionally, the whole accessible 3D spatial frequency region has a donut-shaped distribution, which is manifested by the missing cone problem rooted in transmission measurements as shown earlier in Fig. 2, leaving the center with no frequency information. The missing cone problem can cause the elongation of an object along the z-axis (i.e., the optical axis), thus deteriorating axial resolution. Importantly, this issue results in underestimation of RI values [46,76], which is also a common issue in x-ray CT [77] and magnetic resonance imaging (MRI) [78]. In the case of object rotation TPMs, a complete spatial frequency map can be recovered and thus the missing cone problem can be eliminated if and only if the rotation can fully cover a range of 360° along two axes [29,79,80]. It has also been proposed that by combining angle scanning and sample rotation techniques, one can also fill the whole Ewald sphere to achieve isotropic resolution in TPM [81]. As for the wavelength scanning method, the missing cone problem still exists if the measurements are done in the transmission geometry [32]. In summary, the missing cone problem is difficult to be solved in transmission TPM systems.

Over the past several decades, there has been intensive research work on relieving the missing cone (data) problem and improving the accuracy of reconstructed tomograms mainly in the areas of CT, electron microscope, and MRI [82–84]. Over the past decade, some of the ideas have been innovatively introduced into TPM to significantly enhance the quality of reconstructed RI maps [18,24,42,43,46,48,76]. Basically, all these methods are based on constructing a cost function comprising one quadratic ℓ_2 norm error term and one regularization term, which is expressed as

$$J(f)=\|Af-g\|_{\ell_2}^2+\alpha R(f), \quad (13)$$

where f is the unknown variable to be solved, A is the forward operator characterized by the reconstruction model, Af represents the computed field, g is the measured field, α is the regularization coefficient, and $R(f)$ is the regularization term.

Specifically, for ODT employing the beam scanning method, the error term in the cost function in Eq. (13) can be further expressed as

$$\|Af-g\|_{\ell_2}^2=\sum_m \|A^{(m)}f-g^{(m)}\|_{\ell_2}^2, \quad (14)$$

where m denotes different illumination angles; f corresponds to the scattering potential to be reconstructed (note that earlier we used χ); $A^{(m)}f$ can be interpreted as the mth diffraction projection of f onto the sample plane $z = 0$, which provides a 2D scattering field of a 3D object with respect to the mth incident beam illumination direction unit vector $\hat{\mathbf{k}}_i^{(m)}=(\hat{k}_{xi}^{(m)}, \hat{k}_{yi}^{(m)}, \hat{k}_{zi}^{(m)})$; and $g^{(m)}$ is the mth measured scattered field.

According to the ODT theorem [76], the forward operator can be further specified as a 2D Fourier transform relation

$$A^{(m)}f=\iint \frac{1}{q^{(m)}} f(U,V,W)e^{i(Ux+Vy)}\mathrm{d}U\,\mathrm{d}V, \quad (15)$$

where f is the scattering potential function in the 3D Fourier space (U, V, W) as indicated by its variables, $U=k_x-k_{xi}^{(m)}$, $V=k_y-k_{yi}^{(m)}$, and $W=q^{(m)}-k_{zi}^{(m)}=\sqrt{\beta^2-(U+k_{xi}^{(m)})^2-(V+k_{yi}^{(m)})^2}-k_{zi}^{(m)}$.

The error term in Eq. (13) measures the difference between the computed field and experimentally measured field, and the regularization term imposes certain constraints on the reconstructed image by using prior knowledge of target samples. Then an iterative algorithm is utilized to minimize this cost function until a convergence is reached. The first

used prior information is the non-negativity constraint (NNC), which is grounded in the truth that the difference between the RIs of samples and the surrounding medium should always be non-negative. This method was first demonstrated in TPM by Choi *et al.* in [18] with the missing cone issue significantly reduced compared with when no regularization is imposed. NNC is easy to implement and can always be combined with other methods [76,85]. Later on, the TV regularization method, which measures the total image gradient and possesses stronger constraining effects, has been implemented to TPM [42,46,48]. The TV regularizer has two common variants [86]; one is isotropic TV,

$$\begin{aligned} R_{i\mathrm{TV}}(f) &\equiv \sum_n \|[\nabla f]_n\|_{\ell_2} \\ &= \sum_n \sqrt{([\nabla_x f]_n)^2 + ([\nabla_y f]_n)^2 + ([\nabla_z f]_n)^2}, \end{aligned} \tag{16}$$

and the other is anisotropic TV,

$$\begin{aligned} R_{a\mathrm{TV}}(f) &\equiv \sum_n \|[\nabla f]_n\|_{\ell_1} \\ &= \sum_n (|[\nabla_x f]_n| + |[\nabla_y f]_n| + |[\nabla_z f]_n|). \end{aligned} \tag{17}$$

In Sections 3.A and 3.B, these two TV variants will be discussed in more detail.

A. Isotropic TV

The cost function for an isotropic TV regularizer specifically uses $R_{i\mathrm{TV}}(f)$ as the regularization term. It is not convex due to the TV regularizer term, which makes it impossible to be minimized by a direct gradient descent method. Delaney and Bresler [47] proposed converting this cost function to a half-quadratic version by inserting an auxiliary variable b, following which a global convergence can be reached by alternating minimization with respect to f and b [47]. A fast iterative shrinkage/thresholding algorithm (FISTA), proposed by Beck and Teboulle in [86], relies on efficient evaluation of the gradient of the error term and iteratively solves out the regularization term via a dual optimization approach, where a global rate of convergence is also proven. This algorithm is applicable to both isotropic and anisotropic TV regularizers.

The isotropic TV prior, first introduced by Rudin *et al.* [87] as a constraint imposed on the noises of images, has the capability of denoising, de-blurring, and invasively yielding sharp edges. It works best for piece-wise smooth images that consist of piece-smooth regions separated by sharp edges. In this case, this functional can smooth out noise while well preserving the boundaries [88]. On the other hand, this isotropic TV regularizer can be interpreted as an ℓ_1 penalty on the magnitudes of the image gradient, which bears the sparsity promoting effects on the gradient components of images [89]. This sparsity property has achieved great success in the field of compressive sensing, which recovers images from

insufficiently sampled signals [90]. Kamilov *et al.* in [43] demonstrated that even when the number of measured holograms used for tomogram reconstruction is reduced by a factor of 32, the reconstructed RI map preserves descent quality and similar signal-to-noise ratio. This proves that sparse regularization plays a critical role to significantly enhance the accuracy of the solution to ill-posed inverse problems that are under high under-sampling conditions.

Benefitted from the edge-preserving (EP) characteristic of the isotropic TV regularizer, the so-called EP regularization was proposed by further adding a function to the ℓ_2 norm of the image gradient. Therefore, this regularizer can be formularized as [47,88]

$$R_{EP}(f) \equiv \sum_n \phi(\|[\nabla f]_n\|_{\ell_2}), \tag{18}$$

where ϕ is determined by prior knowledge about sample edges that need to satisfy certain defined conditions. For example, $\phi(t) = T^2 \ln(1 + t/T)$ is one of the choices, where the parameter T can be tuned depending on how sharp the edges need to be kept. Therefore, in the case when sharp edges of samples are highly desired, this functional $\phi(t)$ can be implemented.

Figures 5(a)–5(d) feature a comparison of different regularization methods, including no regularization, NNC, EP regularization, and TV regularization, for 3D RI reconstruction of a hepatocyte cell (the figure is reproduced from [46] with permission). As can be seen in Fig. 5(d), the isotropic TV regularizer can significantly smooth out the noise, while making the edges of the cell's inner structures sharp and clear. Furthermore, the RI values are no longer underestimated compared with the case using no regularization as shown in Fig. 5(a). By sacrificing some noise removal capability, EP regularization, as shown in Fig. 5(c), can further sharpen the edges.

B. Anisotropic TV

The cost function with an anisotropic TV regularizer is very similar to that of the isotropic case, but the regularizer form is replaced with $R_{a\mathrm{TV}}(f)$. This anisotropic TV regularizer can be interpreted as an ℓ_1 penalty directly on the image gradient. It is a very strong regularizer, which offers improvements on reconstruction quality to a great extent compared with the isotropic counterpart [91]. However, its usage is limited to samples whose inner function can be approximated by a piecewise-constant function, thus making it inapplicable to biological samples with complex inner structures. Krauze *et al.* [42] innovatively used this regularizer to retrieve the 3D external geometry of samples, and accordingly made a binary 3D mask to mark out the sample profile. This mask, as the external geometry constraint, can be further applied to existing iterative tomographic reconstruction solvers. Here, the anisotropic TV regularizer can free the retrieved 3D external geometry of the samples from deformation caused by the missing cone problem. Given this prior knowledge, any normal iterative tomographic algorithm can generate a descent reconstruction result with accurate non-piecewise-constant information and correct sample shape.

4. APPLICATIONS

Basically, TPM can noninvasively retrieve the 3D RI distributions of biological samples, providing rich information about live cells without any exogenous contrast agents. Based on the RI maps, both morphological and biochemical information can be further extracted to achieve comprehensive label-free visualization and quantification of livng cells, which opens a new avenue to the investigation of their functionalities and mechanisms at the individual level. The following section will highlight some of the applications of TPM for cellular studies.

A. 3D RI Distribution of Living Cells

Three-dimensional RI mapping of living cells by itself can implicate some pathological states that accompany human diseases. RI distribution has been intensively explored for visualizing the morphological alterations of RBCs caused by parasitic protozoa, such as *P. falciparum* [52,53] and *B. microti* [54]. The human malarial parasite, *P. falciparum*, invades and develops within host human RBCs during the 48-h asexual cycle and can lead to sequestration of RBCs in the microvasculature, which is linked to vital organ dysfunctions under severe malaria conditions [92]. As *P. falciparum* matures and differentiates within a growth-permissive parasitophorous vacuole, the RBCs undergo extensive structural changes, which can be non-invasively monitored by TPM. Figure 6 illustrates the RI maps of *P. falciparum*-invaded human RBCs (Pf-RBCs) during all intra-erythrocytic stages: healthy stage in Fig. 6(a), ring stage in Fig. 6(b), trophozoite stage in Fig. 6(c), and schizont stage in Fig. 6(d) (figures are reproduced from [52] with permission). As shown in Fig. 6(a), healthy RBCs show homogeneous distribution of RI; however, as the stages of parasite development proceed, the Pf-RBCs are becoming more and more optically heterogeneous, as indicated in Figs. 6(b)–6(d). Three main factors contribute to this RI change: (1) the vacuole of the parasite occupies a fraction of the volume in the cytoplasm of the RBCs; the vacuole possesses relatively low RI values as indicated by black arrows in Figs. 6(b)–6(d); (2) hemoglobin (Hb), as the main protein content of RBCs, is digested, metabolized, and converted into hemozoin crystals in the parasite membrane, which have very high RI values as indicated by gray arrows in Figs. 6(c) and 6(d); (3) various parasite proteins are excreted from the parasites into the cytoplasm of the Pf-RBCs [93].

B. Morphological Parameters Accessible by TPM

For the entirety of cells, it is easy for TPM to profile the 3D cell boundary by using the distinct difference of RI values between cells and their surrounding medium; therefore, the morphological parameters over the whole cell scale can be extracted accordingly. Within a cell, the RI distributions of subcellular organelles are also distinguished from the RI distributions of their surrounding cytoplasm; this has enabled TPM to segment out intracellular structures with high accuracy.

1. Cell Entirety Morphology—Given the cell boundary between the intracellular space and surrounding medium, the volume V and surface area A can be effectively calculated for basic and general quantification of cell size. To better extract the cell shape information, different sets of shape parameters can be further adapted. For instance, when the cell shape

is modeled as a 3D ellipsoid, R_1, R_2, and R_3 can be measured as the radii along the three axes in the Cartesian coordinate [94]. On the other hand, if the cell is approximated as a rectangle, the width x and length y can be retrieved to calculate the total edge leading length $L = x + 2y$, which is correlated to cell migration speed and protrusion rate [95]. Nevertheless, after obtaining the basic geometric parameters of cells mentioned above, several dimensional or dimensionless 3D shape descriptors can be further generated to get a higher level sense of cell morphology, which can be potentially linked to significant biological discoveries. For example, surface-to-volume ratio is a typical parameter, which is known to have an influence on the uptake of light, digestion of nutrients, and release of waste of a cell [96]. The compactness $c = 36\pi V^2/A^3$ and sphericity $S = C^{1/3}$ factors, which are parameters used very popularly for evaluating cellular morphological changes, are used to describe how far a cell is from an ideal sphere [97]. The surface area index A/A_S, where A_S is the surface area if the cell is an ideal sphere of the same volume, is often used to describe the deformability of RBCs [98,99].

Thanks to the 3D imaging capability, all these geometric parameters discussed above can be easily obtained by TPM, making it a powerful tool to deeply explore the cells in the morphological world. RBC is one of most popular candidates due to its special biconcave shape and simple inner structures [100–104] [Fig. 7(a)]. Based on the TPM technique, Park *et al.* [100] found out that the volume and surface area of the cord RBCs of newborn infants are much larger than those of the RBCs of non-pregnant women, and these cord RBCs are also flatter than those of adults. By monitoring stored blood without the preservation solution CPDA-1 for around 6 weeks, the 3D RI tomograms showed that RBCs experience significant morphological changes during this storage period, transforming from disco-cytes to echinocytes on day 5 and finally becoming spherocytes after 2 weeks [101]. Quantitatively, the RBC volume, surface area, and sphericity parameters were compared between stored blood with and without CPDA-1 after different storage periods [101]. Besides RBCs, TPM has also been widely utilized to study the morphological features of other types of eukaryotic cells, such as white blood cells [Fig. 7(b)], neurons [Fig. 7(c)], hepatocytes [Fig. 7(d)], phytoplanktons, and cancer cells [26,105,106]. By visualizing neurons treated with the 1-methyl-4-phenylpyridinium ion (MPP+), known to cause Parkinson's disease, for 5 h with the help of 3D RI mapping, it was found that MPP+ can lead to neuron membrane blebs, cytoskeleton disruption, neurite shortening, cell shrinkage, and rounding, which are typically linked to apoptotic morphology and are highly consistent with previous reports using other techniques [107].

2. Subcellular Structures—Since the RI maps of subcellular organelles are also different from those of the surrounding cytoplasm, 3D RI tomograms derived by TPM can effectively retrieve the inner structural boundaries by accurately profiling the isosurfaces of organelles based on RI and gradients of RI information simultaneously. Thanks to the high RI sensitivity of TPM, these subcellular morphological features can add greater value to the study of cellular inner functional activities and biological responses to external stimuli such as drug treatment, osmotic pressure, shear stress, etc.

Under TPM, the most distinguishable subcellular organelles are the nucleoli and the nucleus excluding nucleoli, where the higher RI of nucleoli compared with the remaining part of the

nucleus can be associated with the active ribosomal assembly and rRNA synthesis in the nucleoli [108]. By comparing the nucleus zone of different categories of white blood cells plotted out by RI tomograms, T cells were shown to have a much more spherical shape of the nucleus, in comparison with monocytes and neutrophils. With respect to the ratio of nucleus to cytoplasm volume, T cells are the largest, followed by monocytes, while neutrophils rank the last [79,107,109]. Sung *et al.* [24] distinguished chromosomes from the surrounding cytoplasm in HeLa, HT-29, and T84 cells, so that the chromosomal dry mass can be calculated individually; this can be potentially used to detect chromosomal abnormalities and differentiate cell types in a label-free manner.

LDs are subcellular organelles with important roles in lipid storage and metabolism in most cell types; they are related with various pathologies, including cancer, obesity, and diabetes mellitus [110,111]. However, the underlying mechanisms of growth, movement, and biosynthesis of LDs have not been well understood. The fact that the RI values of LDs are distinctly higher than that of the cytoplasm offers TPM an opportunity to segment out LDs and act as a 3D label-free tool for their imaging and quantification [31,55,112]. Using TPM, Kim *et al.* [55] obtained the time lapse of the 3D RI distributions of LDs inside a hepatocyte cell. By 3D tracking of individual LDs over 93 s, they revealed that the diffusive motions of LDs have a great variety, ranging from sub-diffusion to active transport. This complex 3D dynamic of LDs inside live cells originates from the interaction between LDs and surrounding cellular architectures.

Although possessing high RI sensitivity, conventional TPM still cannot detect very small subcellular organelles with size of less than 400 nm. One of the main reasons is the diffraction-limited lateral and axial resolutions. With the help of a complex deconvolution method that uses an experimentally measured CTF to correct the aberrations of the optical system, one can push the lateral resolution to the sub-100 nm region and improve the axial resolution to 150 nm [45]. Leveraging this significantly improved resolution, subcellular coil-like structures of *Escherichia* bacteria (*Escherichia coli*) can be discerned out [44], and the synaptic network remodeling processes during neuronal development can be monitored, where the growth of thin dendrites (~150 nm) can be precisely measured (~400 nm/min) [45].

C. Biochemical Information Retrievable by TPM

Besides being able to unfold biophysical features, RI maps of living cells can also carry biochemical information about cells. This is due to the established fact that there is a linear relationship between the RI value of a biological sample, n, and the dry mass concentration (or called dry mass density) of organic molecules, C, which can be described by the equation $n = n_m + \alpha C$, where n_m is the RI value of the medium surrounding the sample and α is the refraction increment [113,114]. Fortunately, for the majority of chemical components within a cell, the linear coefficient α relating RI and dry mass concentration remains constant regardless of the chemical identity of the biomaterial [115,116]. More specifically, the mean value of α for the entire set of human proteins is 0.190 ml/g with a standard deviation of only 0.003 ml/g [117]. Therefore, the RI map obtained by TPM can be straightforwardly converted to the dry mass (non-aqueous) concentration, C, which can indeed be viewed as

the concentration of the biochemical components of a cell. As mentioned before, the cell volume parameter can be extracted from the RI map; then, together with the newly introduced dry mass density, the dry mass value that quantifies the total mass of all the non-aqueous contents of a cell can be computed. To make use of the 3D RI map from TPM better, the volume integral of the dry mass density of a specific subcellular organelle (segmented out) can give us the dry mass of that particular organelle. This biochemical parameter is inaccessible through a 2D QPI modality. To be noted, although TPM can measure the total dry mass of all the proteins in cells, it lacks the molecule specificity, that is to say, it cannot quantify the mass for each kind of protein.

The cytoplasm of RBCs is mainly composed of Hb, which is the iron-containing oxygen-transport metalloprotein. The properties of Hb are sensitive to subtle alterations of pathological states of RBCs resulting from infectious diseases and genetic disorders, e.g., malaria and sickle cell diseases [118,119]. To quantify Hb, mean corpuscular Hb concentration (MCHC) and mean corpuscular Hb content (MCH) are being used for medical diagnosis on a daily basis in medical laboratories [120]. MCHC and MCH values can be measured with TPM, which can be used to quantitatively investigate the responses of RBCs to exogenous stimuli or their endogenous functional disorders [52,54,102–104]. By comparing the MCHC and MCH values of RBCs from healthy humans and patients with iron deficiency anemia (IDA), high reticulocyte content, and hereditary spherocytosis, Kim *et al.* [120] found that the IDA RBCs have significantly decreased MCH values, whereas reticulocytes have relatively larger MCH values, which is consistent with the fact that the oxygen carrying capacity of RBCs is primarily determined by the amount of Hb. Interestingly, in all four groups, there are negative correlations between cell MCHC values and volume, and cell surface area and membrane fluctuations [120].

Cell size, balanced by cell growth and division, is an important phenotypic characteristic of any type of cell [121,122]. Although the process of how it is regulated has fascinated generations of biologists, details have remained largely obscure, mainly because accurate measurements at the single-cell level were difficult to carry out [123]. Cell size can be quantified by geometric size, i.e., cell volume, or dry mass. Previous methods can only measure either cell volume or dry mass, and are largely limited to unattached spherical cells. With high image contrast, TPM can conveniently, accurately, and effectively retrieve cell volume and dry mass parameters simultaneously, without any exogenous labeling agents. Even more, the third parameter, dry mass density, can be calculated easily. All these amazing features undoubtedly make TPM a perfect tool for quantifying cell size in the study of cell growth, proliferation, apoptosis, etc. By quantitatively monitoring the dry mass of lymphoblasts and epithelial cells during cell division, Sung *et al.* [124] found out that both cell types maintain a linear relationship between average growth rate and cell mass over the majority of size range. With unprecedented accuracy, they discovered the asymmetry of division, which led to the conclusion that there must be a cell-autonomous size regulator that requires feedback control and couples cell growth to cell cycle. Utilizing TPM to take time-lapse measurements of cell volume, dry mass, and dry mass density of mouse chondrocytes simultaneously, Cooper *et al.* [19] concluded that there are three distinct phases of hypertrophic cell enlargement. More detailed, in phase 1, the dry mass density is maintained, whereas cell volumes increase threefold; then in phase 2, cell volume experiences a fourfold

increase, which is disproportionate with the unchanged rate of dry mass production, thus resulting in a dramatic dilution of dry mass density; finally, in phase 3, dry mass density again stabilizes and cell volume increases another twofold with a proportionate increase in dry mass. This result is remarkable as it reveals the mechanism of cell size increase and the regulation of growth rate [19].

D. Light Scattering Property

Angle- and wavelength-dependent light scattering distributions provide information about the morphological changes accompanying early-stage malignancy of cancers, thus making light scattering a valuable tool for cancer diagnosis over the past decade [125–127]. Light scattering is governed by the complex RI distribution of the samples. Therefore, in order to remodel light scattering in a sample, the 3D RI map is needed, which can be provided by TPM, regardless of various other methods. By modifying the originally measured 3D RI tomograms in a certain way to eliminate the contribution of a specific organelle of interest, the contributions of that specific organelle can be determined and accessed, which can be helpful in diagnosing the precursors of many cancers, where only a certain intracellular organelle, such as the nucleus, undergoes morphological changes [128]. The light scattering analysis, conducted by Hsu *et al.* [129], for instance, showed that the total light scattering cross section and backscattering cross section of cancerous cell lines (CA9-22, BCC) were both significantly higher than those of normal cell lines (HaCaT, SG).

5. CONCLUDING REMARKS

So far, the fundamental physical principles, 3D RI reconstruction algorithms, and various applications of TPM have been thoroughly discussed. Basically, in TPM we solve the inverse scattering problem and reconstruct the 3D RI maps through multiple measurements of complex scattered fields in different ways, such as object rotation, scanning illumination laser beam angles or wavelengths, and sample focus scanning under incoherent illuminations. With 3D Fourier space mapping or BPM, combined with regularization algorithms, accurate 3D RI maps of samples are calculated from TPM data. In addition, starting from the RI distribution, plenty of morphological and biochemical parameters can be retrieved accordingly, which opens the door to cell biology studies. Compared with other 3D imaging modalities, such as confocal microscopy, OCT, and multiphoton microscopy, the 3D quantitative amplitude and phase imaging capability and the label-free characteristic are the most significant features of TPM. As an emerging optical imaging technique, TPM can be used individually or combined with other imaging modalities to effectively and efficiently tackle many unresolved but important biological and medical problems in the future.

Over the past 4 years, it has been exciting to witness the successful promotion of the TPM technique into industry for much wider applications. Two representative cases are NanoLive Inc. (founded in 2013) [45] and TomoCube Inc. (founded in 2016) [130]. Both companies use the angle scanning ODT technique to obtain label-free 3D images of entire cells and tissue slices, and promise to open numerous unexplored applications in biology and medicine. This is the first time that the TPM technique is extended from lab research to

public use, and we believe that TPM's high speed, high resolution, and noninvasive characteristics can soon make it popular among biologists and physicians all over the world.

Although TPM has been intensively developed over the past 10 years, its applications are still limited to cell biology studies; thus, it needs to be fully explored for more translational research. Due to the shortcomings of the currently available methods, many long-standing problems remain in the biomedical field, but they can be potentially solved with TPM. For instance, immunocyte phenotyping, stem cell multipotency identification, cancer cell screening, and tissue pathology are promising directions in which TPM may contribute. However, in order to achieve actual success in these important topics, there still are many important technical issues of TPM waiting to be solved such as throughput and reflection-mode measurement capability.

The biophysical state of a cell is potentially a rich source of information, indicative of cell identity and physiology. Among the various biophysical parameters, mechanical stiffness may serve as predictive markers of cellular fate [131], and nuclear membrane fluctuations have been used to distinguish the multipotent stem cells and mesenchymal stromal cells from osteochondral progenitor subpopulations [132]. For measuring both parameters by TPM, very high lateral and axial resolution and RI sensitivity for accurate cell nucleus segmentation are required. This is one of the significant technical improvement directions for future TPM development.

Besides biophysical properties, the biomolecule information of cells and tissues can also offer us clues about their metabolic activities, thus helping to study the pathophysiology of human diseases and obtain early diagnosis of them [133]. With the help of new light sources with broad wavelength bands and appropriate detectors, TPM can provide a label-free noninvasive spectroscopic approach for assessing the molecular specificity of live cells via optical dispersion [134]. Jung *et al.* [33] demonstrated the first wavelength-dependent 3D RI tomography of cells and used it to quantify the dispersive characteristics of the Hb molecule. We hope that this type of hyperspectral RI dispersion measurement could be used in more important biological or clinical research in the future to provide useful molecular information about live cells and tissues.

One of the ultimate goals of developing various optical imaging techniques is to transfer them from laboratory research to clinics as they become mature enough in the final developing stage. In the past several decades, we have witnessed several successful examples, such as OCT, Raman spectroscopy, PC microscopy, multiphoton microscopy, etc. It is natural to envision that TPM will also gradually step on this path to broaden its applications. However, in order to make TPM really compatible with the already established clinical procedures, at least two main major improvements should be critically addressed: high-throughput feature and *in-vivo* capability. First of all, clinical diagnostics on cells, such as blood testing, usually need to deal with millions of cells to obtain statistical understanding on the cell populations. However, current reported TPM systems in the literature have a very limited field of view (~50 μm × 50 μm), with which only a few cells can be observed in one 3D RI tomogram, and at least tens of measurements are needed to generate one tomogram, which takes a lot of time. As mentioned previously, active illumination schemes using a

DMD or LED array combined with high-speed cameras can accelerate the data acquisition process to potentially solve this problem to a certain extent [31,135]. Nevertheless, a TPM system with a much larger field of view still needs to be developed in order to further enhance imaging throughput in the future. Second, current TPM techniques rely on measuring the scattered fields transmitted from the samples, and, thus, require the illumination part and sensing part of the optical system to be on opposite sides of the samples, which is not suitable for *in-vivo* imaging. To solve this issue, the reflected scattered fields from samples need to be measured for obtaining the 3D tomograms [14,39].

In conclusion, TPM is still in its early stage of development, and has only been applied to a small number of areas in the biomedical field. There are still several important aforementioned directions to make breakthroughs to broaden and deepen TPM applications. We have witnessed rapid growth of this field in the past decade, which in turn consolidates our belief that TPM will undoubtedly play important and even irreplaceable roles in various biomedical studies in the future.

Acknowledgments

Funding. National Institutes of Health (NIH) (1R01HL121386-01A1, NIH9P41EB015871-26A1); Hamamatsu Corp.; Singapore-MIT Alliance for Research and Technology Centre (SMART).

References

1. Goodman JW, Lawrence RW. Digital image formation from electronically detectedholograms. Appl Phys Lett. 1967; 11:77–79.
2. Brown BR, Lohmann AW. Complex spatial filtering with binary masks. Appl Opt. 1966; 5:967–969. [PubMed: 20048989]
3. Zernike F. Phase contrast, a new method for the microscopic observation of transparent objects part II. Physica. 1942; 9:974–986.
4. Cuche E, Bevilacqua F, Depeursinge C. Digital holography for quantitative phase-contrast imaging. Opt Lett. 1999; 24:291–293. [PubMed: 18071483]
5. Dunn GA, Zicha D. Phase-shifting interference microscopy applied to the analysis of cell behavior. Symp Soc Exp Biol. 1993; 47:91–106. [PubMed: 8165581]
6. Dunn GA, Zicha D, Fraylich PE. Rapid, microtubule-dependent fluctuations of the cell margin. J Cell Sci. 1997; 110:3091–3098. [PubMed: 9365279]
7. Cuche E, Marquet P, Depeursinge C. Simultaneous amplitude-contrast and quantitative phase-contrast microscopy by numerical reconstruction of Fresnel off-axis holograms. Appl Opt. 1999; 38:6994–7001. [PubMed: 18324243]
8. Popescu G, Deflores LP, Vaughan JC, Badizadegan K, Iwai H, Dasari RR, Feld MS. Fourier phase microscopy for investigation of biological structures and dynamics. Opt Lett. 2004; 29:2503–2505. [PubMed: 15584275]
9. Ikeda T, Popescu G, Dasari RR, Feld MS. Hilbert phase microscopy for investigating fast dynamics in transparent systems. Opt Lett. 2005; 30:1165–1167. [PubMed: 15945142]
10. Kemper B, von Bally G. Digital holographic microscopy for live cell applications and technical inspection. Appl Opt. 2008; 47:A52–A61. [PubMed: 18239699]
11. Popescu, G. Quantitative Phase Imaging of Cells and Tissues. McGraw-Hill; 2011.
12. Miccio L, Finizio A, Puglisi R, Balduzzi D, Galli A, Ferraro P. Dynamic DIC by digital holography microscopy for enhancing phase-contrast visualization. Biomed Opt Express. 2011; 2:331–344. [PubMed: 21339878]

13. Bhaduri B, Edwards C, Pham H, Zhou RJ, Nguyen TH, Goddard LL, Popescu G. Diffraction phase microscopy: principles and applications in materials and life sciences. Adv Opt Photon. 2014; 6:57–119.
14. Choi Y, Hosseini P, Choi W, Dasari RR, So PTC, Yaqoob Z. Dynamic speckle illumination wide-field reflection phase microscopy. Opt Lett. 2014; 39:6062–6065. [PubMed: 25361156]
15. Yaqoob Z, Yamauchi T, Choi W, Fu D, Dasari RR, Feld MS. Single-shot full-field reflection phase microscopy. Opt Express. 2011; 19:7587–7595. [PubMed: 21503067]
16. Yamauchi T, Iwai H, Yamashita Y. Label-free imaging of intra-cellular motility by low-coherent quantitative phase microscopy. Opt Express. 2011; 19:5536–5550. [PubMed: 21445192]
17. Charriere F, Marian A, Montfort F, Kuehn J, Colomb T, Cuche E, Marquet P, Depeursinge C. Cell refractive index tomography by digital holographic microscopy. Opt Lett. 2006; 31:178–180. [PubMed: 16441022]
18. Choi W, Fang-Yen C, Badizadegan K, Oh S, Lue N, Dasari RR, Feld MS. Tomographic phase microscopy. Nat Methods. 2007; 4:717–719. [PubMed: 17694065]
19. Cooper KL, Oh S, Sung Y, Dasari RR, Kirschner MW, Tabin CJ. Multiple phases of chondrocyte enlargement underlie differences in skeletal proportions. Nature. 2013; 495:375–378. [PubMed: 23485973]
20. Sung YJ, Choi W, Fang-Yen C, Badizadegan K, Dasari RR, Feld MS. Optical diffraction tomography for high resolution live cell imaging. Opt Express. 2009; 17:266–277. [PubMed: 19129896]
21. Wolf E. Three-dimensional structure determination of semi-transparent objects from holographic data. Opt Commun. 1969; 1:153–156.
22. Fiolka R, Wicker K, Heintzmann R, Stemmer A. Simplified approach to diffraction tomography in optical microscopy. Opt Express. 2009; 17:12407–12417. [PubMed: 19654642]
23. Haeberle O, Belkebir K, Giovaninni H, Sentenac A. Tomographic diffractive microscopy: basics, techniques and perspectives. J Mod Opt. 2010; 57:686–699.
24. Sung Y, Choi W, Lue N, Dasari RR, Yaqoob Z. Stain-free quantification of chromosomes in live cells using regularized tomographic phase microscopy. PLoS One. 2012; 7:e49502. [PubMed: 23166689]
25. Kim T, Zhou R, Goddard LL, Popescu G. Solving inverse scattering problems in biological samples by quantitative phase imaging. Laser Photon Rev. 2016; 10:13–39.
26. Kim K, Yoon J, Shin S, Lee S, Yang SA, Park Y. Optical diffraction tomography techniques for the study of cell pathophysiology. J Biomed Photon Eng. 2016; 2:020201.
27. Fang-Yen C, Choi W, Sung YJ, Holbrow CJ, Dasari RR, Feld MS. Video-rate tomographic phase microscopy. J Biomed Opt. 2011; 16:011005. [PubMed: 21280892]
28. KuĹ A, Krauze W. Active limited-angle tomographic phase microscope. J Biomed Opt. 2015; 20:111216. [PubMed: 26361341]
29. Habaza M, Gilboa B, Roichman Y, Shaked NT. Tomographic phase microscopy with 180° rotation of live cells in suspension by holographic optical tweezers. Opt Lett. 2015; 40:1881–1884. [PubMed: 25872098]
30. Chowdhury S, Eldridge WJ, Wax A, Izatt JA. Refractive index tomography with structured illumination. 2017 arXiv:1702.03595.
31. Shin S, Kim K, Yoon J, Park Y. Active illumination using a digital micromirror device for quantitative phase imaging. Opt Lett. 2015; 40:5407–5410. [PubMed: 26565886]
32. Hosseini P, Sung Y, Choi Y, Lue N, Yaqoob Z, So PTC. Scanning color optical tomography (SCOT). Opt Express. 2015; 23:19752–19762. [PubMed: 26367632]
33. Jung J, Kim K, Yoon J, Park Y. Hyperspectral optical diffraction tomography. Opt Express. 2016; 24:2006–2012. [PubMed: 26906777]
34. Lue N, Choi W, Popescu G, Badizadegan K, Dasari RR, Feld MS. Synthetic aperture tomographic phase microscopy for 3D imaging of live cells in translational motion. Opt Express. 2008; 16:16240–16246. [PubMed: 18825263]

35. Dardikman G, Habaza M, Waller L, Shaked NT. Video-rate processing in tomographic phase microscopy of biological cells using CUDA. Opt Express. 2016; 24:11839–11854. [PubMed: 27410107]
36. Sung Y, Lue N, Hamza B, Martel J, Irimia D, Dasari RR, Choi W, Yaqoob Z, So PTC. Three-dimensional holographic refractive-Index measurement of continuously flowing cells in a microfluidic channel. Phys Rev Appl. 2014; 1:014002. [PubMed: 25419536]
37. Agard DA, Hiraoka Y, Shaw P, Sedat JW. Fluorescence microscopy in three dimensions. Methods Cell Biol. 1989; 30:353–377. [PubMed: 2494418]
38. Gustafsson MGL, Shao L, Carlton PM, Wang CJR, Golubovskaya IN, Cande WZ, Agard DA, Sedat JW. Three-dimensional resolution doubling in wide-field fluorescence microscopy by structured illumination. Biophys J. 2008; 94:4957–4970. [PubMed: 18326650]
39. Zhou R, Jin D, Hosseini P, Singh VJ, Kim Y, Kuang CF, Dasari RR, Yaqoob Z, So PTC. Modeling the depth-sectioning effect in reflection-mode dynamic speckle-field interferometric microscopy. Opt Express. 2017; 25:130–143. [PubMed: 28085800]
40. Huang D, Swanson EA, Lin CP, Schuman JS, Stinson WG, Chang W, Hee MR, Flotte T, Gregory K, Puliafito CA, Fujimoto JG. Optical coherence tomography. Science. 1991; 254:1178–1181. [PubMed: 1957169]
41. Kim T, Zhou R, Mir M, Babacan SD, Carney PS, Goddard LL, Popescu G. White-light diffraction tomography of unlabelled live cells. Nat Photonics. 2014; 8:256–263.
42. Krauze W, Makowski P, Kujawinska M, Kus A. Generalized total variation iterative constraint strategy in limited angle optical diffraction tomography. Opt Express. 2016; 24:4924–4936. [PubMed: 29092320]
43. Kamilov US, Papadopoulos IN, Shoreh MH, Goy A, Vonesch C, Unser M, Psaltis D. Optical tomographic image reconstruction based on beam propagation and sparse regularization. IEEE Trans Comput Imaging. 2016; 2:59–70.
44. Mir M, Babacan SD, Bednarz M, Do MN, Golding I, Popescu G. Visualizing Escherichia coli sub-cellular structure using sparse deconvolution spatial light interference tomography. PLoS One. 2012; 7:e39816. [PubMed: 22761910]
45. Cotte Y, Toy F, Jourdain P, Pavillon N, Boss D, Magistretti P, Marquet P, Depeursinge C. Marker-free phase nanoscopy. Nat Photonics. 2013; 7:113–117.
46. Lim J, Lee K, Jin KH, Shin S, Lee S, Park Y, Ye JC. Comparative study of iterative reconstruction algorithms for missing cone problems in optical diffraction tomography. Opt Express. 2015; 23:16933–16948. [PubMed: 26191704]
47. Delaney AH, Bresler Y. Globally convergent edge-preserving regularized reconstruction: an application to limited-angle tomography. IEEE Trans Image Process. 1998; 7:204–221. [PubMed: 18267394]
48. Kamilov US, Papadopoulos IN, Shoreh MH, Goy A, Vonesch C, Unser M, Psaltis D. Learning approach to optical tomography. Optica. 2015; 2:517–522.
49. Waller L, Tian L. Computational imaging: machine learning for 3D microscopy. Nature. 2015; 523:416–417. [PubMed: 26201593]
50. Yoon J, Kim K, Park H, Choi C, Jang S, Park Y. Label-free characterization of white blood cells by measuring 3D refractive index maps. Biomed Opt Express. 2015; 6:3865–3875. [PubMed: 26504637]
51. Majeed H, Sridharan S, Mir M, Ma L, Min E, Jung W, Popescu G. Quantitative phase imaging for medical diagnosis. J Biophoton. 2017; 10:177–205.
52. Park Y, Diez-Silva M, Popescu G, Lykotrafitis G, Choi W, Feld MS, Suresh S. Refractive index maps and membrane dynamics of human red blood cells parasitized by Plasmodium falciparum. Proc Natl Acad Sci USA. 2008; 105:13730–13735. [PubMed: 18772382]
53. Chandramohanadas R, Park Y, Lui L, Li A, Quinn D, Liew K, Diez-Silva M, Sung Y, Dao M, Lim CT, Preiser PR, Suresh S. Biophysics of malarial parasite exit from infected erythrocytes. PLoS One. 2011; 6:e20869. [PubMed: 21698115]
54. Park H, Hong SH, Kim K, Cho SH, Lee WJ, Kim Y, Lee SE, Park Y. Characterizations of individual mouse red blood cells parasitized by Babesia microti using 3-D holographic microscopy. Sci Rep. 2015; 5:10827. [PubMed: 26039793]

55. Kim K, Lee S, Yoon J, Heo J, Choi C, Park Y. Three-dimensional label-free imaging and quantification of lipid droplets in live hepatocytes. Sci Rep. 2016; 6:36815. [PubMed: 27874018]
56. Snyder R, Hesselink L. High-speed optical tomography for flow visualization. Appl Opt. 1985; 24:4046–4051. [PubMed: 18224160]
57. Devaney AJ. A computer simulation study of diffraction tomography. IEEE Trans Biomed Eng. 1983; BME-30:377–386.
58. Devaney AJ. Inverse-scattering theory within the Rytov approximation. Opt Lett. 1981; 6:374–376. [PubMed: 19701437]
59. Maleki MH, Devaney AJ. Phase-retrieval and intensity-only reconstruction algorithms for optical diffraction tomography. J Opt Soc Am A. 1993; 10:1086–1092.
60. Kozacki T, Kujawińska M, Kniażewski P. Investigation of limitations of optical diffraction tomography. Opto-Electron Rev. 2007; 15:102–109.
61. Zhou R, Kim T, Goddard LL, Popescu G. Inverse scattering solutions using low-coherence light. Opt Lett. 2014; 39:4494–4497. [PubMed: 25078211]
62. Sheppard CJR, Gu M, Mao XQ. Three-dimensional coherent transfer function in a reflection-mode confocal scanning microscope. Opt Commun. 1991; 81:281–284.
63. Gu, M. Principles of Three Dimensional Imaging in Confocal Microscopes. World Scientific; 1996. p. 337
64. Chew, WC. IEEE Press Series on Electromagnetic Waves. IEEE; 1995. Waves and Fields in Inhomogeneous Media; p. 608
65. Somekh MG, See CW, Goh J. Wide field amplitude and phase confocal microscope with speckle illumination. Opt Commun. 2000; 174:75–80.
66. Redding B, Bromberg Y, Choma MA, Cao H. Full-field interferometric confocal microscopy using a VCSEL array. Opt Lett. 2014; 39:4446–4449. [PubMed: 25078199]
67. Kolman P, Chmelík R. Coherence-controlled holographic microscope. Opt Express. 2010; 18:21990–22004. [PubMed: 20941100]
68. Witte S, Plauşka A, Ridder MC, van Berge L, Mansvelder HD, Groot ML. Short-coherence off-axis holographic phase microscopy of live cell dynamics. Biomed Opt Express. 2012; 3:2184–2189. [PubMed: 23024912]
69. Kollarova V, Collakova J, Dostal Z, Vesely P, Chmelik R. Quantitative phase imaging through scattering media by means of coherence-controlled holographic microscope. J Biomed Opt. 2015; 20:111206. [PubMed: 26244853]
70. Nguyen TH, Majeed H, Popescu G. Plane-wave decomposition of spatially random fields. Opt Lett. 2015; 40:1394–1397. [PubMed: 25831341]
71. Wiener N. Generalized harmonic analysis. Acta Math. 1930; 55:117–258.
72. Khintchine A. Korrelationstheorie der stationären stochastischen Prozesse. Math Ann. 1934; 109:604–615.
73. Choi Y, Yang TD, Lee KJ, Choi W. Full-field and single-shot quantitative phase microscopy using dynamic speckle illumination. Opt Lett. 2011; 36:2465–2467. [PubMed: 21725446]
74. Tian L, Waller L. 3D intensity and phase imaging from light field measurements in an LED array microscope. Optica. 2015; 2:104–111.
75. Vanroey J, Vanderdonk J, Lagasse PE. Beam-propagation method—analysis and assessment. J Opt Soc Am. 1981; 71:803–810.
76. Sung Y, Dasari RR. Deterministic regularization of three-dimensional optical diffraction tomography. J Opt Soc Am A. 2011; 28:1554–1561.
77. Rangayyan R, Dhawan AP, Gordon R. Algorithms for limited-view computed tomography: an annotated bibliography and a challenge. Appl Opt. 1985; 24:4000–4012. [PubMed: 18224155]
78. Weerasinghe C, Yan H. An improved algorithm for rotational motion artifact suppression in MRI. IEEE Trans Med Imaging. 1998; 17:310–317. [PubMed: 9688164]
79. Habaza M, Kirschbaum M, Guernth-Marschner C, Dardikman G, Barnea I, Korenstein R, Duschl C, Shaked NT. Rapid 3D refractive-index imaging of live cells in suspension without labeling using dielectrophoretic cell rotation. Adv Sci. 2016; 4:1600205.

80. Kou SS, Sheppard CJ. Image formation in holographic tomography: high-aperture imaging conditions. Appl Opt. 2009; 48:H168–H175. [PubMed: 19956288]
81. Vertu S, Flügge J, Delaunay JJ, Haeberlé O. Improved and isotropic resolution in tomographic diffractive microscopy combining sample and illumination rotation. Open Phys. 2011; 9:969–974.
82. Bartolac S, Clackdoyle R, Noo F, Siewerdsen J, Moseley D, Jaffray D. A local shift-variant Fourier model and experimental validation of circular cone-beam computed tomography artifacts. Med Phys. 2009; 36:500–512. [PubMed: 19291989]
83. Oliva MV, Muhammed HH. New approach for limited-angle problems in electron microscope based on compressed sensing. Engineering. 2013; 05:575–578.
84. Jin J, Liu F, Crozier S. Image registration guided, sparsity constrained reconstructions for dynamic MRI. Magn Reson Imaging. 2014; 32:1403–1417. [PubMed: 25131631]
85. Babacan, SD., Molina, R., Katsaggelos, AK. Sparse Bayesian image restoration. IEEE International Conference on Image Processing; 2010. p. 3577-3580.
86. Becker SR, Combettes PL. Fast gradient-based algorithms for constrained total variation image denoising and deblurring problems. J Nonlinear Convex Anal. 2014; 15:137–159.
87. Rudin LI, Osher S, Fatemi E. Nonlinear total variation noise removal algorithm. Physica D. 1992; 60:259–268.
88. Charbonnier P, Blanc-Feraud L, Aubert G, Barlaud M. Deterministic edge-preserving regularization in computed imaging. IEEE Trans Image Process. 1997; 6:298–311. [PubMed: 18282924]
89. Unser, M., Tafti, PD. An Introduction to Sparse Stochastic Processes. Cambridge University; 2014.
90. Candes EJ, Romberg J, Tao T. Robust uncertainty principles: exact signal reconstruction from highly incomplete frequency information. IEEE Trans Inf Theory. 2006; 52:489–509.
91. Jin, X., Li, L., Chen, ZQ., Zhang, L., Xing, YX. Anisotropic total variation for limited-angle CT reconstruction. IEEE Nuclear Science Symposium Conference Record (NSS/MIC); 2010. p. 2232-2238.
92. Miller LH, Baruch DI, Marsh K, Doumbo OK. The pathogenic basis of malaria. Nature. 2002; 415:673–679. [PubMed: 11832955]
93. Tilley L, McFadden G, Cowman A, Klonis N. Illuminating Plasmodium falciparum-infected red blood cells. Trends Parasitol. 2007; 23:268–277. [PubMed: 17434344]
94. Gul-Mohammed J, Arganda-Carreras I, Andrey P, Galy V, Boudier T. A generic classification-based method for segmentation of nuclei in 3D images of early embryos. BMC Bioinf. 2014; 15:9.
95. Keren K, Pincus Z, Allen GM, Barnhart EL, Marriott G, Mogilner A, Theriot JA. Mechanism of shape determination in motile cells. Nature. 2008; 453:475–480. [PubMed: 18497816]
96. Lewis WM. Surface/volume ratio: implications for phytoplankton morphology. Science. 1976; 192:885–887. [PubMed: 17817763]
97. Mohandas N, Gallagher PG. Red cell membrane: past, present, and future. Blood. 2008; 112:3939–3948. [PubMed: 18988878]
98. Linderkamp O, Wu PY, Meiselman HJ. Geometry of neonatal and adult red blood cells. Pediatr Res. 1983; 17:250–253. [PubMed: 6856385]
99. Chien S. Red cell deformability and its relevance to blood flow. Annu Rev Physiol. 1987; 49:177–192. [PubMed: 3551796]
100. Park H, Ahn T, Kim K, Lee S, Kook SY, Lee D, Suh IB, Na S, Park Y. Three-dimensional refractive index tomograms and deformability of individual human red blood cells from cord blood of newborn infants and maternal blood. J Biomed Opt. 2015; 20:111208. [PubMed: 26259511]
101. Kim K, Choe K, Park I, Kim P, Park Y. Holographic intravital microscopy for 2-D and 3-D imaging intact circulating blood cells in microcapillaries of live mice. Sci Rep. 2016; 6:33084. [PubMed: 27605489]
102. Lee S, Park H, Jang S, Park Y. Refractive index tomograms and dynamic membrane fluctuations of red blood cells from patients with diabetes mellitus. Blood. 2016; 128:4813.

103. Kim K, Yoon H, Diez-Silva M, Dao M, Dasari RR, Park Y. High-resolution three-dimensional imaging of red blood cells parasitized by Plasmodium falciparum and in situ hemozoin crystals using optical diffraction tomography. J Biomed Opt. 2014; 19:011005. [PubMed: 23797986]
104. Lee SY, Park HJ, Best-Popescu C, Jang S, Park YK. The effects of ethanol on the morphological and biochemical properties of individual human red blood cells. PLoS One. 2015; 10:e0145327. [PubMed: 26690915]
105. Kus A, Dudek M, Kemper B, Kujawinska M, Vollmer A. Tomographic phase microscopy of living three-dimensional cell cultures. J Biomed Opt. 2014; 19:046009. [PubMed: 24723114]
106. Su JW, Hsu WC, Chou CY, Chang CH, Sung KB. Digital holographic microtomography for high-resolution refractive index mapping of live cells. J Biophoton. 2013; 6:416–424.
107. Yang S-A, Yoon J, Kim K, Park Y. Measurements of morphological and biochemical alterations in individual neuron cells associated with early neurotoxic effects in Parkinson's disease. 2016 bioRxiv 080937V2.
108. Hsu WC, Su JW, Tseng TY, Sung KB. Tomographic diffractive microscopy of living cells based on a common-path configuration. Opt Lett. 2014; 39:2210–2213. [PubMed: 24686713]
109. Kim K, Yoon J, Park Y. Simultaneous 3D visualization and position tracking of optically trapped particles using optical diffraction tomography. Optica. 2015; 2:343–346.
110. Martin S, Parton RG. Lipid droplets: a unified view of a dynamic organelle. Nat Rev Mol Cell Biol. 2006; 7:373–378. [PubMed: 16550215]
111. Greenberg AS, Coleman RA, Kraemer FB, McManaman JL, Obin MS, Puri V, Yan QW, Miyoshi H, Mashek DG. The role of lipid droplets in metabolic disease in rodents and humans. J Clin Invest. 2011; 121:2102–2110. [PubMed: 21633178]
112. Lee S, Kim K, Mubarok A, Panduwirawan A, Lee K, Lee S, Park H, Park Y. High-resolution 3-D refractive index tomography and 2-D synthetic aperture imaging of live phytoplankton. J Opt Soc Korea. 2014; 18:691–697.
113. Barer R. Interference microscopy and mass determination. Nature. 1952; 169:366–367. [PubMed: 14919571]
114. Barer R, Tkaczyk S. Refractive index of concentrated protein solutions. Nature. 1954; 173:821–822. [PubMed: 13165653]
115. Mir M, Wang Z, Shen Z, Bednarz M, Bashir R, Golding I, Prasanth SG, Popescu G. Optical measurement of cycle-dependent cell growth. Proc Natl Acad Sci USA. 2011; 108:13124–13129. [PubMed: 21788503]
116. Handwerger KE, Cordero JA, Gall JG. Cajal bodies, nucleoli, and speckles in the *Xenopus* oocyte nucleus have a low-density, sponge-like structure. Mol Biol Cell. 2004; 16:202–211. [PubMed: 15509651]
117. Zhao H, Brown PH, Schuck P. On the distribution of protein refractive index increments. Biophys J. 2011; 100:2309–2317. [PubMed: 21539801]
118. Hosseini P, Abidi SZ, Du E, Papageorgiou DP, Choi Y, Park Y, Higgins JM, Kato GJ, Suresh S, Dao M, Yaqoob Z, So PT. Cellular normoxic biophysical markers of hydroxyurea treatment in sickle cell disease. Proc Natl Acad Sci USA. 2016; 113:9527–9532. [PubMed: 27512047]
119. Mills JP, Diez-Silva M, Quinn DJ, Dao M, Lang MJ, Tan KS, Lim CT, Milon G, David PH, Mercereau-Puijalon O, Bonnefoy S, Suresh S. Effect of plasmodial RESA protein on deformability of human red blood cells harboring Plasmodium falciparum. Proc Natl Acad Sci USA. 2007; 104:9213–9217. [PubMed: 17517609]
120. Kim Y, Shim H, Kim K, Park H, Jang S, Park Y. Profiling individual human red blood cells using common-path diffraction optical tomography. Sci Rep. 2014; 4:6659. [PubMed: 25322756]
121. Moseley JB, Mayeux A, Paoletti A, Nurse P. A spatial gradient coordinates cell size and mitotic entry in fission yeast. Nature. 2009; 459:857–860. [PubMed: 19474789]
122. Martin SG, Berthelot-Grosjean M. Polar gradients of the DYRK-family kinase Pom1 couple cell length with the cell cycle. Nature. 2009; 459:852–856. [PubMed: 19474792]
123. Jorgensen P, Tyers M. How cells coordinate growth and division. Curr Biol. 2004; 14:R1014–R1027. [PubMed: 15589139]

124. Sung Y, Tzur A, Oh S, Choi W, Li V, Dasari RR, Yaqoob Z, Kirschner MW. Size homeostasis in adherent cells studied by synthetic phase microscopy. Proc Natl Acad Sci USA. 2013; 110:16687–16692. [PubMed: 24065823]

125. Boustany NN, Boppart SA, Backman V. Microscopic imaging and spectroscopy with scattered light. Annu Rev Biomed Eng. 2010; 12:285–314. [PubMed: 20617940]

126. Wang Z, Tangella K, Balla A, Popescu G. Tissue refractive index as marker of disease. J Biomed Opt. 2011; 16:116017. [PubMed: 22112122]

127. Lee K, Kim HD, Kim K, Kim Y, Hillman TR, Min B, Park Y. Synthetic Fourier transform light scattering. Opt Express. 2013; 21:22453–22463. [PubMed: 24104134]

128. Kalashnikov M, Choi W, Yu CC, Sung Y, Dasari RR, Badizadegan K, Feld MS. Assessing light scattering of intracellular organelles in single intact living cells. Opt Express. 2009; 17:19674–19681. [PubMed: 19997187]

129. Hsu WC, Su JW, Chang CC, Sung KB. Investigating the backscattering characteristics of individual normal and cancerous cells based on experimentally determined three-dimensional refractive index distributions. Proc SPIE. 2012; 8553:85531O.

130. Shin S, Kim K, Kim T, Yoon J, Hong K, Park J, Park Y. Optical diffraction tomography using a digital micromirror device for stable measurements of 4D refractive index tomography of cells. 2016 arXiv:1602.03294.

131. Van Vliet KJ, Bao G, Suresh S. The biomechanics toolbox: experimental approaches for living cells and biomolecules. Acta Mater. 2003; 51:5881–5905.

132. Lee WC, Shi H, Poon Z, Nyan LM, Kaushik T, Shivashankar GV, Chan JK, Lim CT, Han J, Van Vliet KJ. Multivariate biophysical markers predictive of mesenchymal stromal cell multipotency. Proc Natl Acad Sci USA. 2014; 111:E4409–E4418. [PubMed: 25298531]

133. Ntziachristos V. Fluorescence molecular imaging. Annu Rev Biomed Eng. 2006; 8:1–33. [PubMed: 16834550]

134. Jung J, Kim K, Yu H, Lee K, Lee S, Nahm S, Park H, Park Y. Biomedical applications of holographic microspectroscopy [invited]. Appl Opt. 2014; 53:G111–G122. [PubMed: 25322118]

135. Zuo C, Sun J, Zhang J, Hu Y, Chen Q. Lensless phase microscopy and diffraction tomography with multi-angle and multi-wavelength illuminations using a LED matrix. Opt Express. 2015; 23:14314–14328. [PubMed: 26072796]

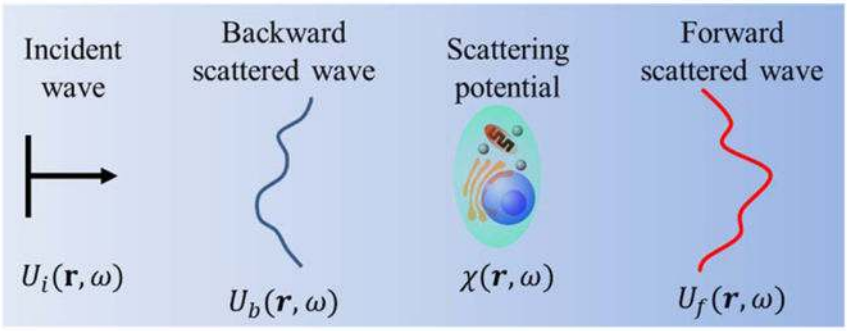

Fig. 1.
Illustration of optical diffraction tomography. (Figure reprinted from Ref. [61] with permission.)

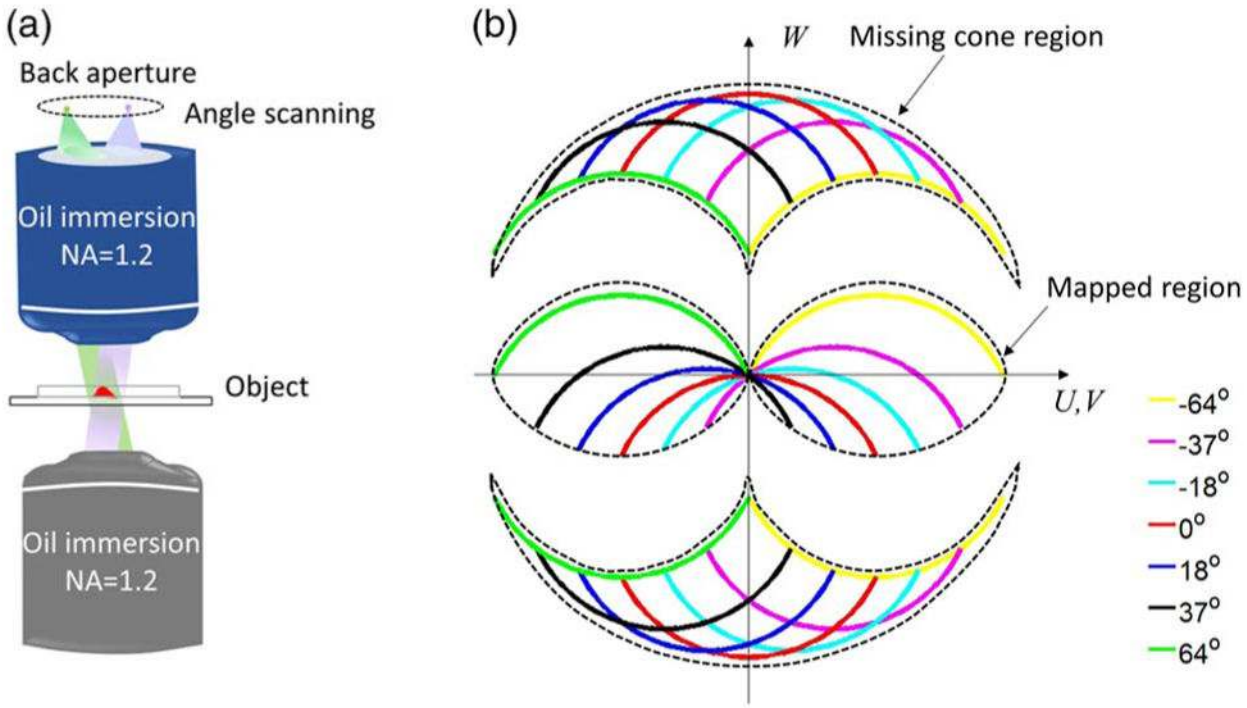

Fig. 2.
Illustration of angle scanning-based scattered field measurements and frequency domain mapping.

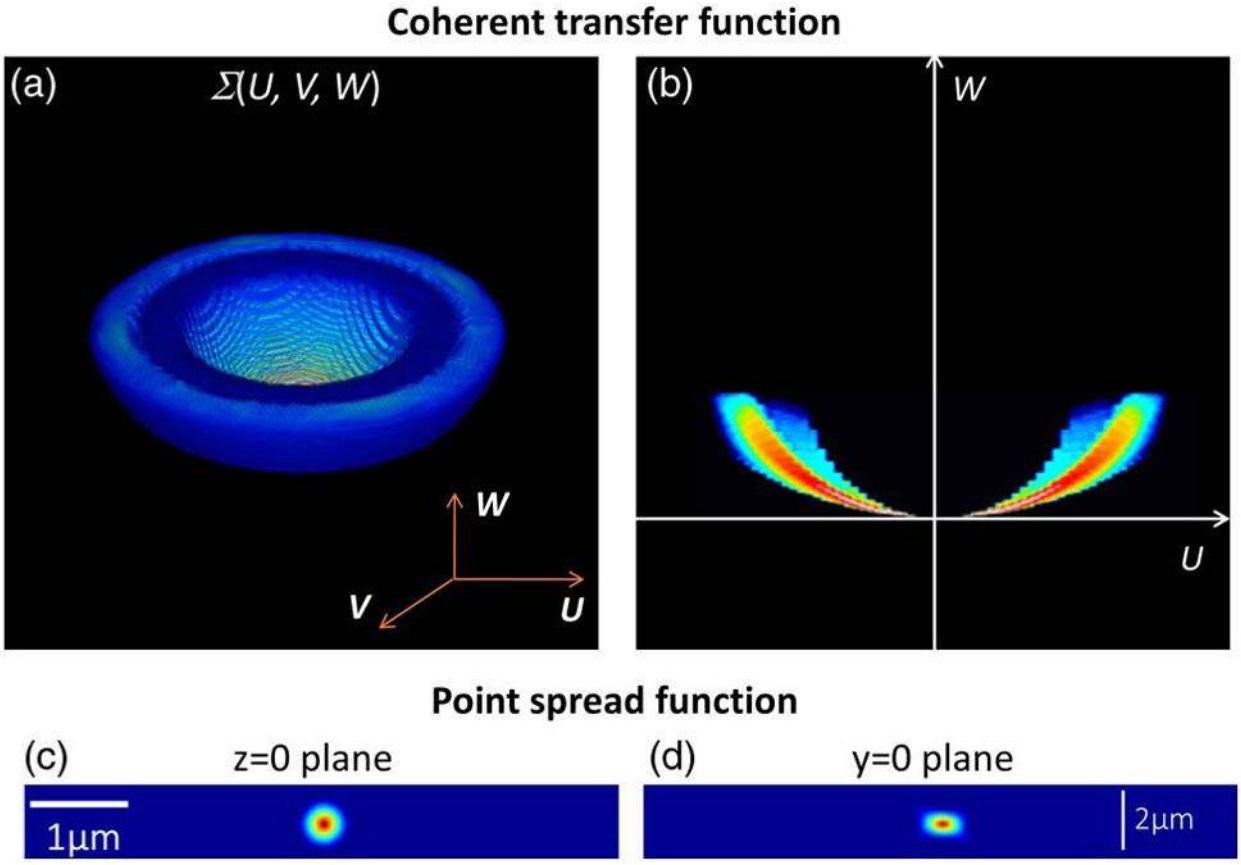

Fig. 3.

Temporally incoherent ODT reconstruction illustration. (a) Coherent transfer function. (b) The 3D PSF in x–y ($z = 0$) and x–z ($y = 0$) planes obtained from the CTF. (Figure reprinted from Ref. [41].)

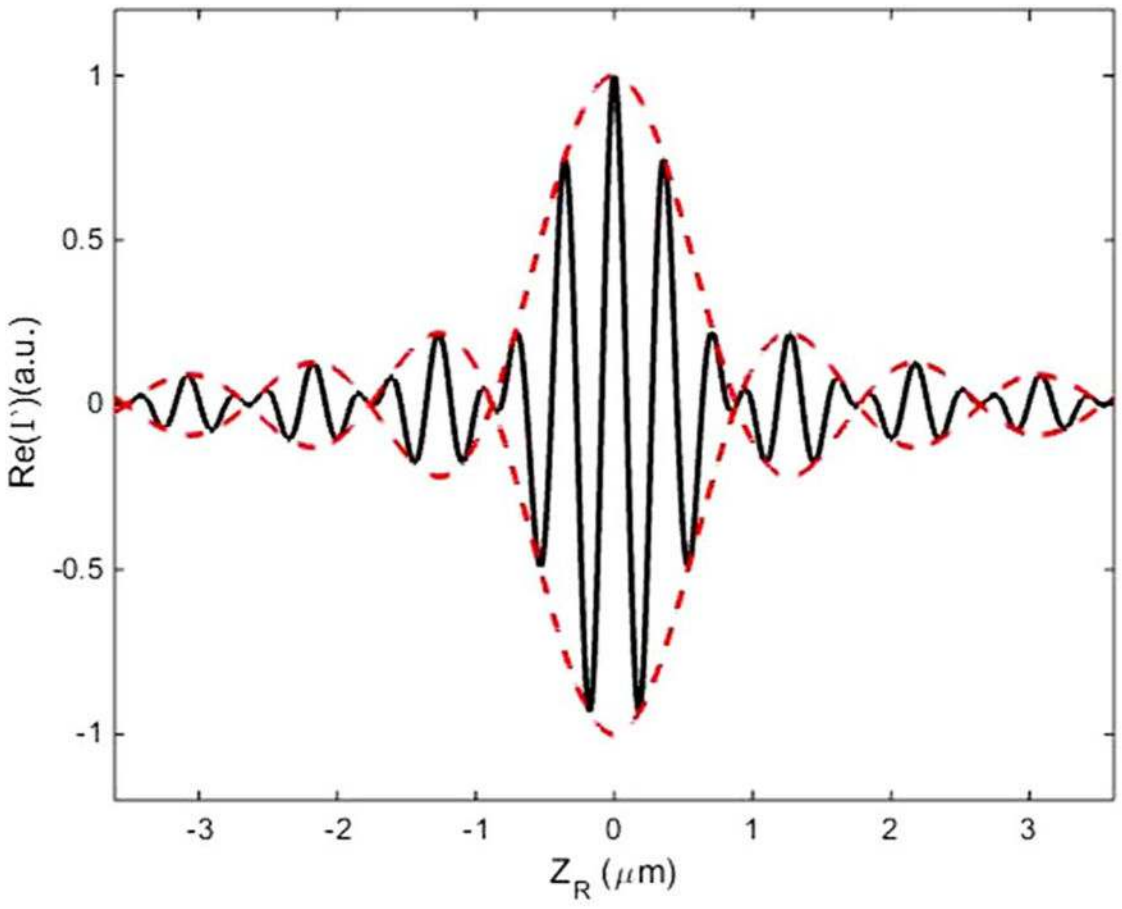

Fig. 4.
Overall spatial correlation function for 800 nm speckle illumination with NA = 1.0. (Figure reprinted from Ref. [39] with permission.)

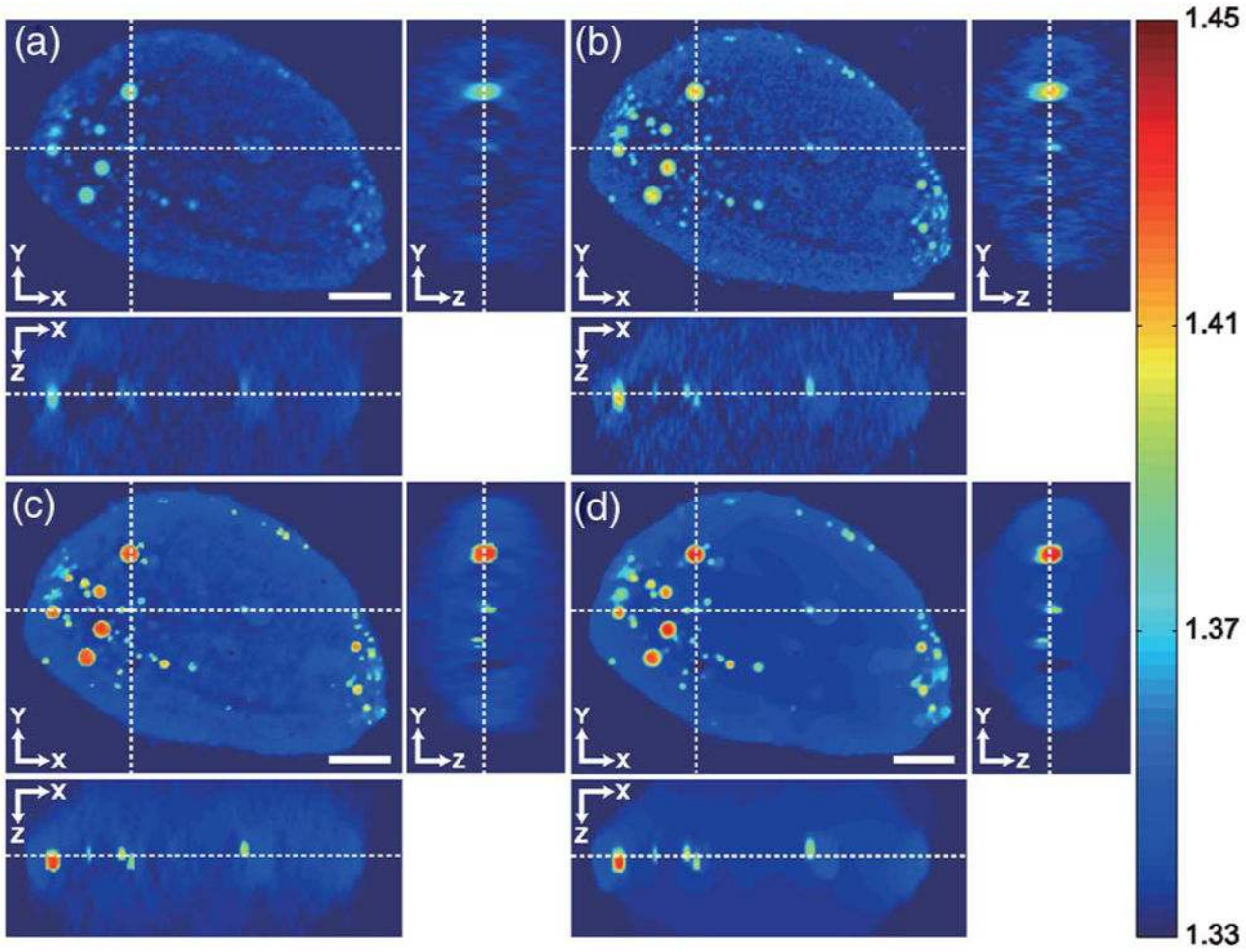

Fig. 5.

Comparison of the 3D RI distribution of a hepatocyte cell reconstructed by (a) direct Fourier mapping, (b) NNC, (c) EP regularization, and (d) isotropic TV regularization. (Figure reprinted from Ref. [46] with permission.)

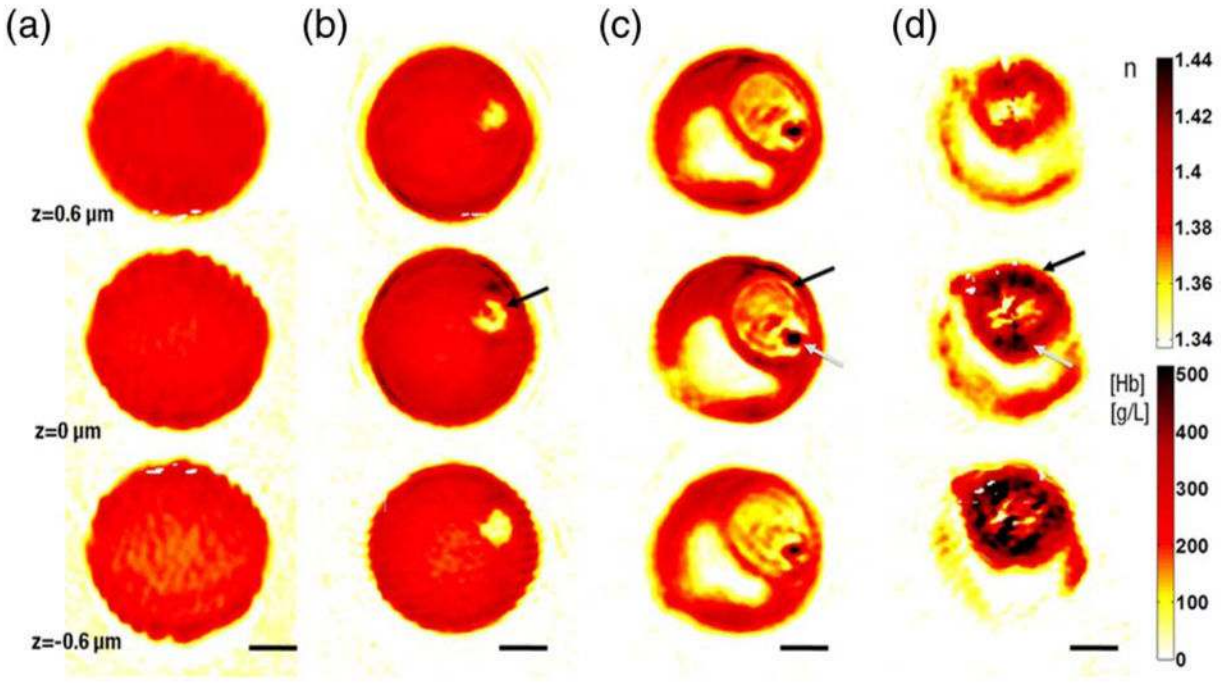

Fig. 6.

3D RI maps of Pf-RBCs during all intra-erythrocytic stages: (a) healthy RBCs, (b) ring stage, (c) trophozoite stage, (d) schizont stage. Images in rows show three different *x*–*y* cross sections: 0.6 μm above the focused plane (top), on the focused plane (middle), and 0.6 μm below the focused plane (bottom). Two color maps show the RI (top right) and Hb concentration (bottom right) (scale bar, 1.5 μm). (Figure reprinted from Ref. [52] with permission. Copyright (2008) National Academy of Sciences, U.S.A.)

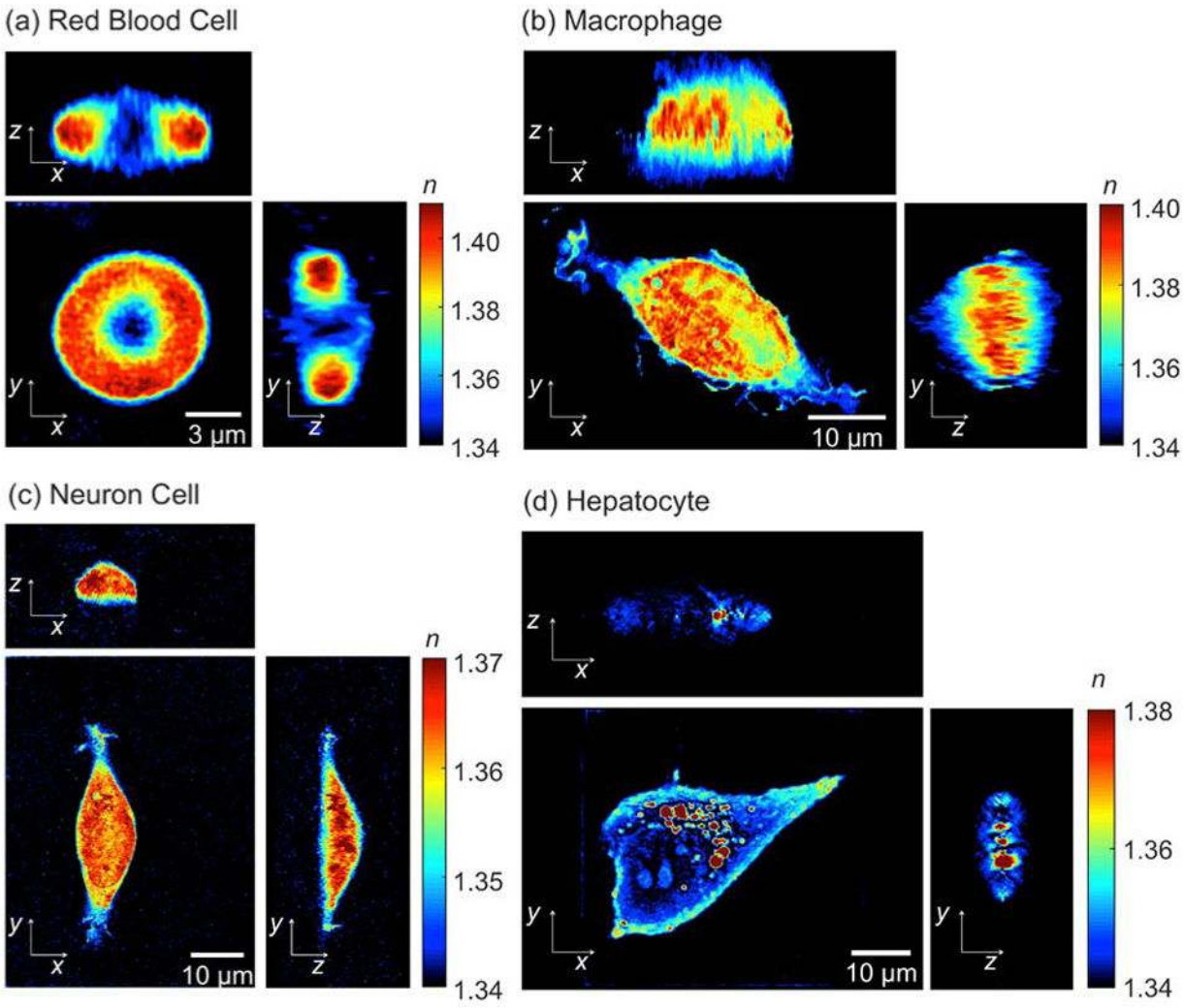

Fig. 7.

Representative 3D RI tomograms of (a) an RBC, (b) a macrophage, (c) a neuron, and (d) a hepatocyte. (Figures reprinted from Ref. [26] with permission.)